Experimental techniques for multi-scale description of soil fabric and its dual pore network

Enrique Romero*-Guido Musso-Cristina Jommi*****

** Universitat Politècnica de Catalunya*
Department of Geotechnical Engineering and Geosciences
c/ Jordi Girona, 1-3, Campus Nord UPC, Building D-2
08034 Barcelona, Spain
enrique.romero-morales@upc.edu

***Politecnico di Torino*
Dipartimento di Ingegneria Strutturale, Edile e Geotecnica
Corso Duca degli Abruzzi, 24
10129 Torino, Italy

****Politecnico di Milano*
Dipartimento di Ingegneria Strutturale
piazza Leonardo da Vinci, 32
20133 Milano, Italy

Fabric affects many aspects of soil mechanical behaviour. When transport processes are of concern, its dual, the pore network, is the key aspect ruling the soil properties of interest. In this chapter, a review of a few widely used techniques, currently adopted to analyse the pore network at increasing scale, is presented, namely mercury intrusion porosimetry, environmental scanning electron microscopy and electrical resistivity tomography. Details on the techniques, their advantages and limitations, are first covered, followed by the presentation of selected test results. The results highlight how these techniques provide an insight into the pore network, and how they can be usefully exploited in the understanding of different hydro-electro-mechanical processes ordinarily observed at the phenomenological scale. Attention is focused on unsaturated soils with reference to water retention properties, micro / macrostructure interaction, and role of sample heterogeneity.

1 Introduction

Multi-scale studies associated with pore network properties are increasingly used to improve understanding of behaviour features and multiphase flow properties in porous media at the phenomenological scale, where the latter term is used to identify the scale of a standard laboratory test on a representative *homogeneous* volume element. These include distribution of pores space –micropore / macropore-, connectivity, constricted porosity by throats, hysteresis, fluid occupancy during multiphase flow displacement processes, wettability. Pore network rules liquid and gas permeability properties, as well as water retention, and electro-chemical transport. Dually, it affects mechanical properties, among which volumetric stiffness may be mentioned. As will be shown in the next chapter, flow and deformation properties are therefore coupled, and influence each other.

The pore network is studied at the microstructure scale, by means of techniques at the particle / aggregation scale (usually below <100 μm) capable of analysing the arrangement and distribution of particles and pores –and their contacts and connectivity– [Del96, Mit05, And12]. Among various available techniques used to study porous geomaterials at the microstructural scale, mercury intrusion porosimetry (MIP) and scanning electron microscopy (environmental ESEM with digital image analysis) are given special attention in the present chapter. The former technique has been frequently used to describe pore network properties affecting coupled hydro-chemo-mechanical processes (see, for instance, [AlM96, Rom99, Mus03, Kol06b, Rom11]). The latter is a quantitative technique with minimal sample preparation requirement, and which allows subjecting the sample to hydraulic paths during observation [Mon03a, Mon03b, Rom08, Air10].

Mesostructural scanning techniques, based on time-domain reflectometry, near-infrared spectroscopic measurements, electric impedance/resistivity tomography, neutron tomography, X-ray computed tomography, dual-energy gamma-ray technique, among others, allow increasing the scale of observation, therefore appreciating the role of heterogeneous elements, such as inclusions or cracks, in the engineering behaviour of porous media [Bak90, Bor05, Des06, And12]. Applications of these mesostructural techniques in saturated and unsaturated soils have been devoted to the monitoring of hydro-chemo-mechanical processes [Com08, Com10, Dam09, Cos12], to the detection of desiccation cracks [Geb06, Muk06, Sen09], to the visualisation of diffusion and multiphase transport processes, as well as fluid retention and permeation properties [Rol05, Van05, Rod06, Car06, Kol06a, Pir07, Kar07, Man12, Rie12]. Higher resolution mesostructural techniques, together with improved image processing, have recently allowed moving to micrometric scale, narrowing the gap between meso and microstructural techniques [Bri98, Jac02, Bés06, Tak06, And12].

Among the latter mesostructural technique, electrical resistivity tomography (ERT) is described in detail in this chapter. The technique turns out to be remarkably useful when studying coupled hydro-chemo-mechanical phenomena in which the pore network arrangement, and not only the pore size distribution, plays a relevant role.

The spatial resolution of ERT as a mesostructure tool is slightly above 10 mm. At this resolution, and with reference to geomaterials testing, it can be classified as a semi-quantitative technique, since it provides a good general electrical picture of the sample, while accuracy in estimating electrical conductivity can be lost if sharp gradients exists. With respect to other techniques mentioned before, an essential advantage of ERT is that it can be easily implemented in modified laboratory cells for mechanical and hydraulic testing. Sequences of maps of electrical resistivity (potentially 3D), taken while performing hydro-chemo-mechanical tests, can then be used to visualize transport and mechanical processes occurring inside the sample. Appropriate data treatment may be exploited to back-analyse transport parameters, as shown in the last chapter.

2 Mercury intrusion porosimetry and environmental scanning electron microscopy

2.1 Mercury intrusion porosimetry

Mercury intrusion porosimetry (MIP) is one of the most commonly used techniques for analysing the pore size distribution (PSD) of geomaterials with interconnected porosity. The interested reader may refer to [Web97, Del96, Sim04, Rom08]. With this technique an absolute pressure p is applied to a non-wetting liquid (mercury) in order to enter the empty pores. Washburn equation may be adopted to provide a relationship between the applied pressure and a characteristic size of the intruded pores [Dia70, Jua86]. For ideal pores of cylindrical shape or parallel infinite plates (fissure-like pores), the equation reads:

$$p = -\frac{n\,\sigma_{Hg}\cos\theta_{nw}}{x} \tag{1}$$

where σ_{Hg} is the surface tension of mercury (σ_{Hg}=0.484 N/m at 25°C), θ_{nw} the contact angle between mercury and particles surface, and x the entrance or throat pore diameter ($n = 4$) or the spacing width between parallel plates ($n = 2$). The value $n = 4$ is often used in MIP, as the cylindrical model is most frequently adopted. The contact angle is usually taken between 139° and 147° for clay minerals [Dia70], although higher values have been reported on kaolinitic clay [Pen00].

Sample preparation requires emptying the sample of water that prevents the penetration of mercury. Samples can be dehydrated using controlled relative humidity-drying, oven-drying, freeze-drying or critical-point-drying techniques [Del84b]. For heat and dry sensitive materials, freeze drying is preferred [Ahm74]. Freeze drying process involves temperature (fast cooling) and pressure conditions (sublimation of

ice) to avoid surface tension forces caused by air-water interfaces [Ahm74, Del82, Del84b, Del96, Pen00].

A constant contact angle at equilibrium is assumed in the elaboration of MIP data, irrespective of the actual penetration flow conditions, in spite of Equation (1) being valid only with reference to equilibrated states, at null penetration velocity of mercury. In fact, the contact angle varies as a function of the dynamic flow of the advancing interface, as shown by [Hof75, Aït04]. For this reason, sufficient time lapse must be left in pressure rising and mercury ejection to allow for quasi-static state conditions to be reached at any step. Usually, an imposed mercury pressure is held constant until penetration ceases or falls below a specified rate.

The main limitations of MIP are: a) completely isolated pores enclosed by surrounding solids are not measured –this enclosed porosity is not significant in soils, but can play increasing role in low-porosity geomaterials-; b) pores that are accessible only through smaller ones, hence constricted porosity by throat effect, are not detected until the smaller entrance pores are penetrated; c) the apparatus may not have enough capacity to enter the smallest pores of the sample (non-intruded porosity with entrance pore sizes below 7 nm); and d) the minimum pressure which can be applied practically by the apparatus limits the maximum detected pore size (non-detected porosity with entrance pore sizes larger than 400 μm). Alteration in the pore geometry during pressure application is also of concern. It has been reported that the soil structure is not affected during high-pressure intrusion [Sil73, Law78 and Ree79], due to the fact that most of the pore network is already filled with incompressible mercury during penetration. However, this is not the case before penetration starts and at low applied pressure, for compressible materials. Occurrence of substantial initial volume change due to isotropic compression in clayey samples prior to intrusion was reported by [Pen00]. Deformation of the sample holder system during mercury pressure changes is another factor which can induce interpretation errors, and which should be accounted for in data elaboration [Sim04].

The pore-size distribution can be deduced by mercury intrusion, by relating the volume of intruded pores to the pressure required for intrusion. The intrusion stage can be followed by an extrusion stage, which can be accomplished by decreasing the applied pressure. The cumulative intruded volume data along an intrusion-extrusion cycle highlights that not all the mercury intruded during the penetration stage is recovered when the pressure is released. An amount of mercury remains permanently entrapped in the constricted porosity by throat effects. Various theories explaining the causes of MIP hysteresis and entrapment have been discussed and examined in detail by [Mat95, Abe99 and Mor02]. A second intrusion will follow approximately the same extrusion path, thus identifying that part of porosity which is not affected by throat effects. The latter is assumed to coincide with the non-constricted or free porosity. Delage & Lefebvre [Del84] and Delage *et al*. [Del96] assumed that the small intra-aggregate pores, pores inside soil aggregates, display a non-constricted or free porosity, while the large inter-aggregate pore space between the aggregates corresponds to the entrapped porosity. The extrusion data can thus be exploited also

to provide additional information on the multiscale arrangement of the microstructure pore network.

Data from mercury intrusion can be complemented, for pore sizes below 60 nm, with nitrogen desorption isotherms (although the use of the adsorption branch is also possible. Data from the latter technique are interpreted using BJH model [Bar51], based on which emptying of pores from condensed adsorptive at decreasing relative nitrogen pressure is re-interpreted by Kelvin equation [Sil73, Web97]. The model is based on the assumption that pores have cylindrical shape and that the pore radius is equal to the sum of the Kelvin radius and the thickness of the film adsorbed on the pore wall.

Results of MIP technique may be better reported as pore size density function, PSD, i.e. the log differential intrusion curve *vs*. entrance or throat pore size, which aids visual detection of the dominant pore modes. Figure 1 shows the cumulative intruded pore ratio (volume of intruded pores / volume of solids) for dense clay phyllite (void ratio around 0.34), as well its corresponding PSD, obtained by MIP and BJH desorption data [Gar10]. According to MIP data, the dense material displays a single dominant pore mode at around 15 nm. PSD based on the analysis of the nitrogen desorption branch is not always straightforward, since an intense spike at around 4nm is sometimes present that reflects an artefact (associated with the spontaneous evaporation of metastable pore liquid, [Low04]). In such cases, a more realistic PSD can be obtained from the analysis of the adsorption branch [Low04].

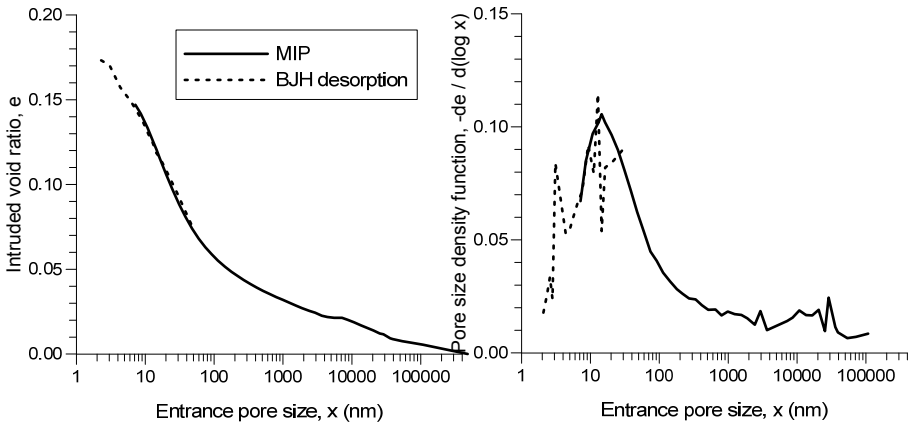

Figure 1: Left: Evolution of intruded void ratio with entrance pore size by MIP and BJH desorption of natural phyllite. Right: Pore size density functions [Gar10].

Further insight into the pore structure may be provided by the interpretation of MIP data in terms of the fractal character of the porous medium, admitting self-similarity of the hierarchical pore network. For the calculation of the surface fractal dimension

D_s, the following expression written as a function of the mercury pressure p, has been usually adopted [Kor92, Mey94, Fad96], where V is the intruded pore volume:

$$\log\left(\frac{\mathrm{d}V}{\mathrm{d}p}\right) \propto (D_s - 4)\log p \tag{2}$$

Intervals of self-similarity of the different pore types can be experimentally obtained from the linear sections of the corresponding log-log plot, the slope of which gives the values of D_s, as shown in Figure 2. In the figure, one pressure range is identified for the high-density soil with a characteristic fractal dimension of D_s=3.09, which reflects a more space-filling volumetric pore structure. On the contrary, two pressure regimes can be identified in the low-density sample: a low-pressure regime exhibiting a fractal dimension D_s=1.88, which corresponds to a fissure-like structure, and a high-pressure regime for pore sizes lower than 300 nm presenting again a volumetric structure (D_s = 3.04). Fractal concepts related to porosimetry studies have been used by [Fad96, Gim97, Jom03], as a complementary tool to detect microstructural changes and differences in pore geometry at various structural levels. It is worth noting that fractal dimension analysis also allows detecting anomalies in MIP data, such as the initial compression before mercury penetration takes place.

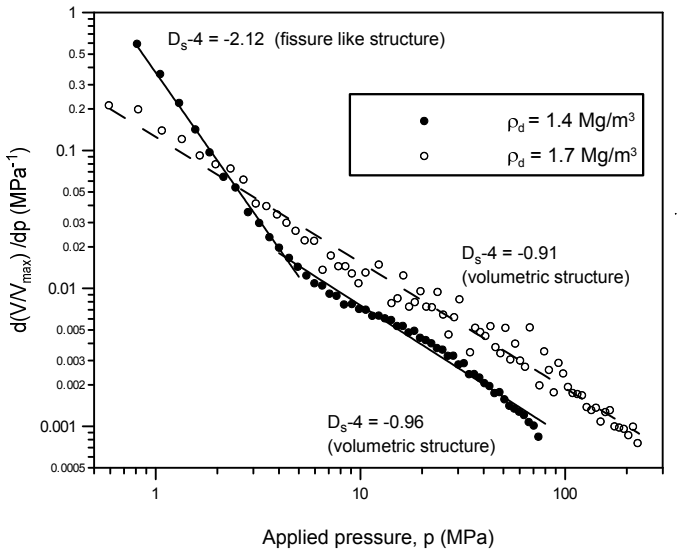

Figure 2: Fractal description of the pore network for two dry densities of a kaolinitic-illitic clay [Rom08].

As MIP data depend on pore sizes and pore network connectivity, they can be usefully exploited to derive quantitative water retention properties of geomaterials [Pra85, Rom99, Aun01, Sim01, Sim02]. The non-wetting mercury penetration at intrusion pressure p is assumed to be equivalent to air-intrusion at matric suction s during a drying path for the same diameter of pores x being intruded:

$$s = \frac{4\sigma \cos\theta_w}{x} \;;\; p = -\frac{4\sigma_{Hg} \cos\theta_{nw}}{x} \;;\; s = -\frac{\sigma \cos\theta_w}{\sigma_{Hg} \cos\theta_{nw}} p \approx 0.196\, p \qquad (3)$$

where σ is the surface tension of water and $\cos\theta_w$=1 the wetting coefficient for the air-water interface (refer to Equation (1) for σ_{Hg} and θ_{nw}).

The volume of pores not intruded by mercury –assuming a non-deformable soil– is used to evaluate the water content w or degree of saturation S_r corresponding to the equivalent applied matric suction. Derivation of the matric suction – saturation relationship from MIP data should be limited to the low-suction range, in which capillarity dominates water retention. In fact, water is generally held due to capillarity at low suctions (usually < 2 MPa), and by adsorption on particle surfaces and in clay inter-layers at higher suctions [Cas92, Rom99]. Moreover, to correctly estimate the water content, data must be corrected for the non-intruded porosity, which can be assimilated to a residual water content w_r [Rom08]:

$$S_{r\,nw} + S_r = 1 \;;\quad (w - w_r) = (w_{sat} - w_r)(1 - S_{r\,nw}) \qquad (4)$$

where w_{sat} is the water content at S_r=1, and $S_{r\,nw}$ the complementary non-wetting degree of saturation intruded by mercury.

In comparing MIP elaboration with direct water retention data, attention must be paid to the evolution of the pore size distribution during hydraulic paths for active soils [Sim01, Sim05, Rom11]. In principle, the PSD measured on a soil sample gives the water retention curve corresponding to the end of a water retention curve test, after volume changes have ceased. Figure 3 presents a comparison of water retention results on drying of a clayey silt, with the information deduced from MIP using freeze-dried samples.

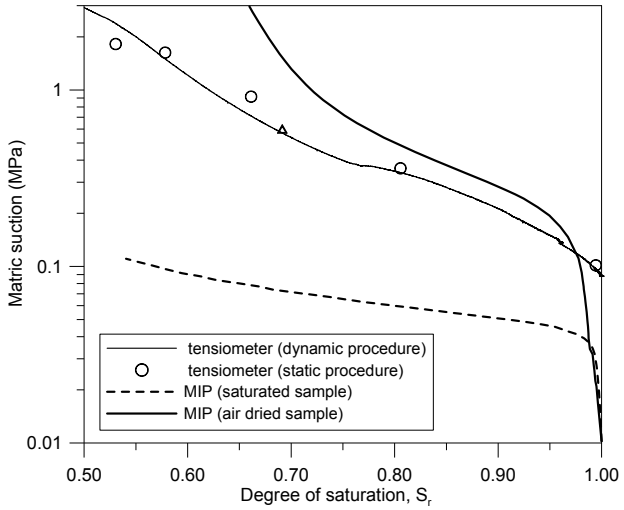

Figure 3: Water retention results on drying of clayey silt compared to deduced data from MIP using freeze-dried samples [Rom08].

'Dynamic' and 'static' procedures refer to the measurement of matric suction using high-range tensiometers during a continuous drying process and at static equilibrium under constant water content, respectively. The figure shows good agreement in the determination of the air-entry value using MIP, when the sample has been previously air-dried and undergone shrinkage. In this case, the denser state reached on drying is associated with a higher air-entry value, which matches the tensiometer results with a distribution of pores that evolve with suction. On the contrary, deduced water retention results from MIP starting from saturated conditions, reflect a lower air entry value, which is in agreement with the *frozen* higher porosity of the saturated state.

MIP results have been successfully used on an extended range (up to 41 MPa) to determine water retention properties of low-porosity claystone (void ratio e=0.12), which does not undergo important volume changes on drying. Figure 4 shows the cumulative intruded void ratio using MIP and BJH adsorption information up to e=0.10. The PSD function obtained from MIP displays one dominant pore mode at approximately 16 nm. The air entry value corresponding to the dominant pore mode can be determined from Laplace's equation, giving a value of 18 MPa. Figure 4 also shows the estimated water retention curve based on MIP deduced data, together with psychrometric measurements.

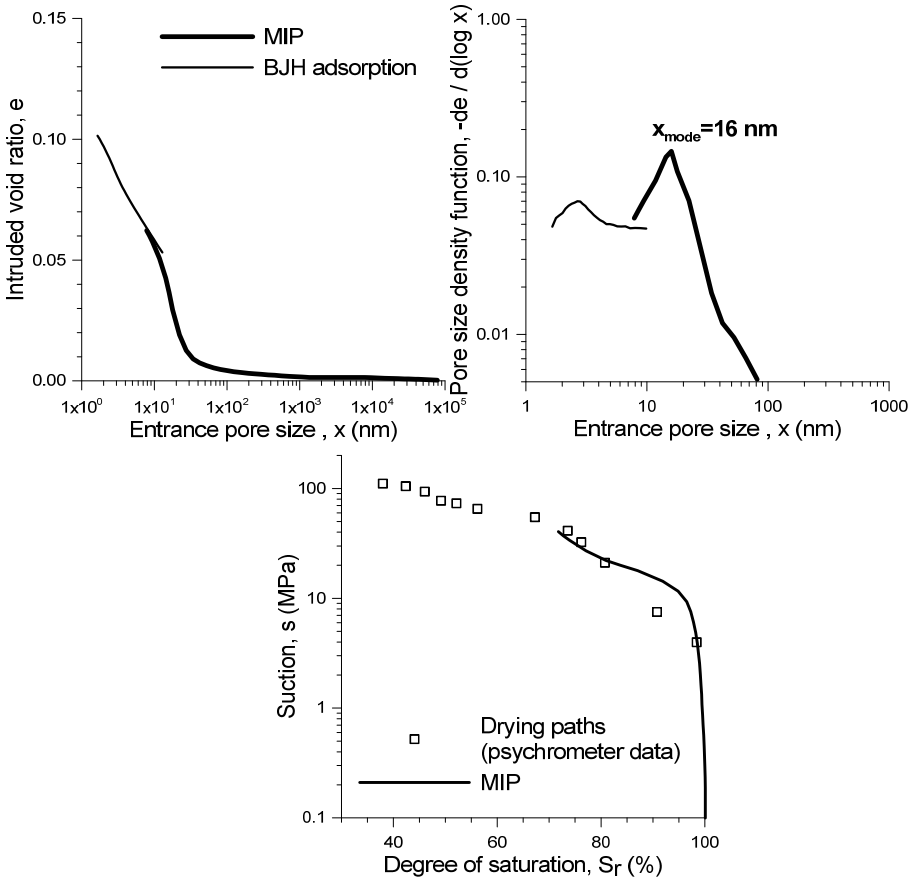

Figure 4: Top left: Cumulated intruded void ratio on low-porosity claystone. Top right: Pore size density function with dominant pore mode. Bottom: Deduced water retention data from MIP results compared to psychrometer readings [Rom12].

2.2 **Environmental scanning electron microscopy**

As already described, MIP analysis is performed on a dried sample, therefore having *frozen* PSD and pore network during the test. On the contrary, the pore network of active soils evolves, together with aggregate swelling and shrinking, when in contact with water. This evolution may be observed by means of Environmental scanning electron microscope (ESEM). The latter is a special type of SEM that works under controlled environmental conditions and requires no conductive coating on the specimen. The technique enables examining wet samples and preserving their natural characteristics for further testing [Dan93, Bak95, Kom99, Mon03a, Rom08, Air10, Rom11].

The equipment presents a sample chamber at a higher pressure and separated from increasing vacuum chambers by pressure-limiting apertures (electron gun chamber is at 10^{-5} Pa). Water vapour is the most commonly used chamber gas, which is controlled with an electronic servo system at absolute vapour pressures between 0.13 and 2 kPa. The microscope is also equipped with a Peltier cooling / heating system (working within 20°C above or below ambient temperature) installed underneath the sample stub to control sample temperature. Accordingly, the examination of the sample can be continuously done at different vapour pressures and temperatures, hence at different relative humidity, making it a suitable equipment to study the gradual effects of wetting and drying stages at microstructural scale. A certain degree of resolution is compromised when using this equipment, especially at elevated relative humidity of the sample chamber.

Montes-H *et al*. [Mon03a, Mon03b] used ESEM jointly with a digital image analysis program to estimate at aggregate scale the swelling–shrinkage behaviour of bentonite at different total suctions. More recently, [Rom08, Air10, Rom11] used the same technique to study the effects of total suction changes on the volumetric behaviour at microstructural level of different clays. Airò Farulla *et al*. [Air10] changed temperature and vapour pressure conditions to perform a suction cycle according to the wetting and drying paths outlined in Figure 5. The cycle started at point B, where the sample (initially at point A), was let to equilibrate for 15 min at RH=30% (total suction around 160 MPa), by applying a vapour pressure of 0.65 kPa at 20°C. A photomicrograph was taken at each stage (different points in Figure 5) and after an equalisation time of 10 minutes. Two procedures for digital image analysis were used to isolate aggregates and calculate area variations due to relative humidity changes. The first procedure, shown in Figure 6, consisted in defining the aggregate contour on the inverse image, in transforming it into a binary image, and in counting the white pixels. Aggregate area variations were calculated with reference to the initial condition (point B, Figure 5). The second procedure used an automatic digital image analysis [Abr04], which consisted in using a threshold filter, in selecting a region of interest and in applying an automatic segmentation algorithm. Aggregate areal deformations (negative in expansion) measured during the wetting and drying cycle and using the two aforementioned procedures are plotted against total suction in Figure 7.

Romero *et al*. [Rom11] used the same procedure to study aggregate volume changes along a wetting and drying cycle on two different clays. A consistent picture of volume change behaviour was obtained by these authors on different clays, when comparing microstructural ESEM results with MIP data and with phenomenological (at larger scale) results. They finally exploited these data to complement the description of evolutionary water retention properties of active clays.

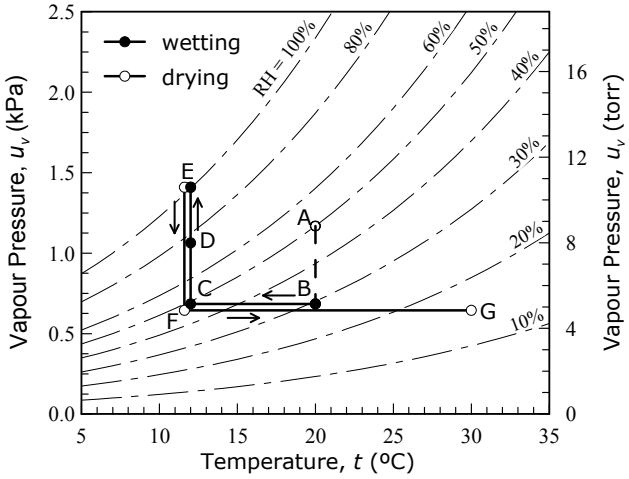

Figure 5: Wetting and drying paths followed by a clayey aggregate in the ESEM [Air10].

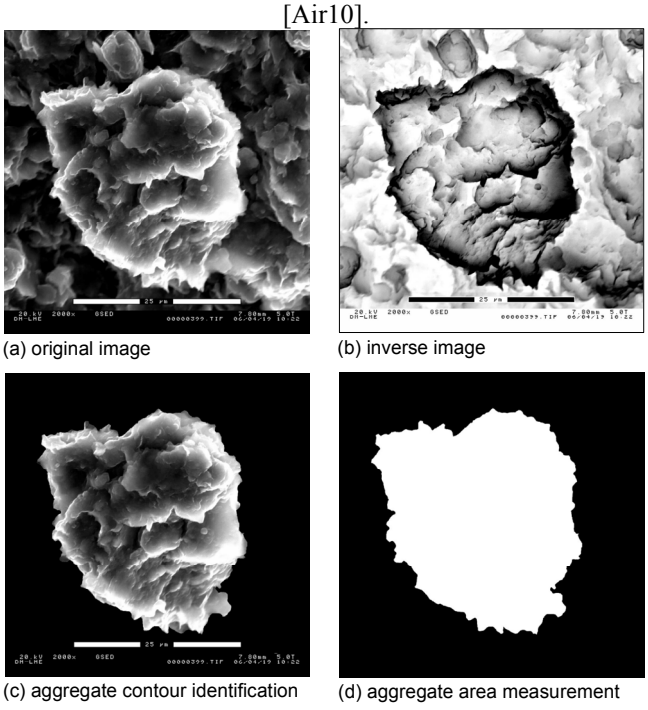

Figure 6: Manual digital image treatment to measure changes in aggregate area. [Air10].

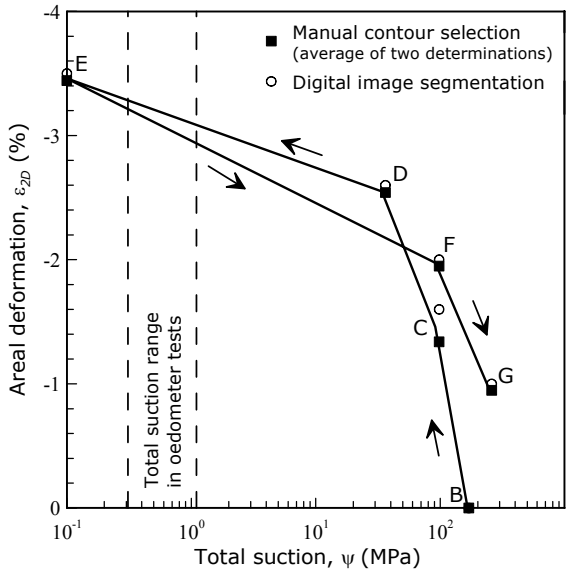

Figure 7: Areal deformation of the aggregate versus total suction in wetting-drying path [Air10].

3 Electrical Resistivity Tomography (ERT)

3.1 Introduction

Electrical resistivity tomography (ERT) allows increasing the scale of observation of the role of pore network on the phenomenological behaviour of soils. Usefulness of electrical measurements in the characterisation of geomaterials at the laboratory scale is enhanced by its association to the tomography technique. A single electrical measurement implicitly introduces the assumption that the investigated body is homogeneous. A great number of measurements, all referring to the same volume but taken from different points, permits the relaxation of the homogeneity assumption. Joint analysis of several measurements allows then an insight into the distribution of electrical properties within the studied body.

Thanks to this scale of observation, ERT may found different applications, among which developments for medical diagnosis are of outmost relevance. As for the literature related to geosciences, the synthetic study from [Lyt78] proved that the technique could be applied as an experimental procedure to detect heterogeneities of rock cores. Since then, the numerical algorithms used have been improved, increasing accuracy in the evaluation of local values of conductivity and resolution in the reconstruction of shapes.

The technique can be applied at different scales (from laboratory mesostructural investigations to stratigraphic characterisation) and the resolution varies from about one millimetre to the order of meters.

In petroleum engineering electrical tomography has been implemented commercially with names such as FMS (Formation MicroScanner) and FMI (Fullbore Formation MicroImager). It is used to obtain 'image logs', or electrical pictures of the wellbore that are quite effective to recognize and detect mechanical failures and naturally occurring fractures. A comparison between information recovered through visual inspection of the core and information from FMS images is available in [Kho12]. The technique is used also to recover stratigraphic information in shallow environments.

In near surface geophysics, early studies included identification of aquifers systems and sources of pollutions [Whi94, Osi95, Bev91]: then attention switched towards imaging of subsurface fluid movement in porous and fractured media [Dai92, Sla97]. Later studies, associated to further improvements of the inversion technique, deal with quantitative assessment of transport characteristics in soils and rocks.

In the following, equipment, operational principles and data elaboration are presented, to highlight the multiscale potentialities of ERT, together with its resolution limitations at the different scales of observation. Microresistivity for fabric studies, which complement the previous techniques, are then introduced. Examples of quantitative application of the technique for multiphase flow are postponed to the last chapter.

3.2 Principles of ERT

In ERT several pairs of electrodes are attached to the surface of the object: two electrodes apply the electrical current, and other pairs of electrodes measure the induced electrical potential differences (as in the four electrodes terminals). Either the pair of electrodes applying current or the pair electrodes measuring the potential drop are changed from measurement to measurement. A forward model is separately built to calculate the electrical potential differences that would be measured if the electrical conductivity within the object had a certain distribution. Finally an inverse model is used to estimate the distribution of electrical conductivity that minimizes the scatter between experimental measurements and predictions of the forward model [Bor05].

ERT reconstruction: forward model

The solution of the forward problem links the voltage measurements to the object conductivity. Most reconstruction codes implement the forward model with a Finite

Element solver [Vau97, Bor02, Pol02], discretising both domain Ω and conductivity distribution.

Assuming that the conductivity χ of the object under measurement is isotropic, that the electric and magnetic fields are slowly varying and neglecting capacitance effects, it follows that the governing equation of the problem is the balance of electrical charge in stationary conditions:

$$\nabla \cdot \left(\chi \nabla \phi \right) = 0 \tag{5}$$

where ϕ is electric potential inside the body.

The presence of the electrodes is taken into account via appropriate conditions at the boundaries of the object, ∂Ω, as with the complete electrode model [Som92]. The model assumes that the potential is homogeneous over the electrode space and that overpotential phenomena occur at the interface between the electrode and the object under measurement. The following relation holds for each electrode *l = 1, ..., L*:

$$V_l = \phi + z_l \chi \frac{\partial \phi}{\partial \vec{n}} \quad on \quad \partial\Omega_l, \quad l = 1,..,L \tag{6}$$

where V_l is potential of the l^{th} electrode, z_l is contact impedance of the l^{th} electrode, $\partial \vec{n}$ is the outwards normal to $\partial\Omega$ and $\partial\Omega_l$ is the portion of $\partial\Omega$ underneath electrode *l*.

Electrical stimuli are accounted for by specifying for each electrode that:

$$\int \chi \frac{\partial \phi}{\partial \vec{n}} = I_l \quad on \quad \partial\Omega_l, \quad l = 1,..,L \tag{7}$$

where I_l is current injected into the l^{th} electrode. Equation (6) and (7) apply to the portions of ∂Ω that fall underneath each electrode. To the remaining parts of ∂Ω (inter electrode gaps), the following relationship applies:

$$\chi \frac{\partial \phi}{\partial \vec{n}} = 0 \tag{8}$$

as no current density is crossing the free surface of the object under measurement. Equations (6) to (8) specify the model for the electrodes, voltages on the electrodes are however specified to within an arbitrary additive constant as no reference potential has been specified. As this is an arbitrary choice, usually the model is complemented with the additional condition:

$$\sum_{l=1}^{L} V_l = 0 \tag{9}$$

that allows the unique determination of all V_l.

ERT reconstruction: inversion

Field reconstruction is formulated as non-linear least-squares problem, where the conductivity of the forward model is varied until a satisfactory match between the measurements simulated by the forward model and the real measurements is met. The reconstruction procedure searches for a discretised conductivity $\mathbf{s}_{rec}$:

$$\mathbf{s}_{rec} = \arg\min \left\| h(\mathbf{s}) - \mathbf{v} \right\|_2^2 \tag{10}$$

where h is the nonlinear forward operator from model space to measurements space, $\mathbf{s}$ is the discrete conductivity, $\mathbf{v}$ is the vector of measured voltages and $\| \ \|_2^2$ indicates the squared 2-norm. The reconstruction problem, both in its continuous form and in its discrete form (Equation 10), is ill-posed in the sense that small perturbations in the measured data can cause arbitrarily large errors in the estimated conductivity [Syl87]. Then, regularisation techniques are needed to obtain a stable solution. In practical terms, ill-conditioning arises from certain patterns of conductivity for which the corresponding measurements are extremely small [Bre90], so being affected by measurement noise. Such patterns of conductivity, for which the observations are unreliable, corrupt the reconstruction. Regularisation techniques are adopted in order to prevent such problem. Commonly Equation (10) is solved using the Tikhonov regularisation, formulating the reconstruction as:

$$\mathbf{s}_{rec} = \arg\min \left\| h(\mathbf{s}) - \mathbf{v} \right\|_2^2 + \alpha F(\mathbf{s}) \tag{11}$$

where $F(\mathbf{s}) > 0$ is the regularisation function, and α a positive scalar called Tikhonov factor. F acts as a penalty term, by taking large values corresponding to distributions $\mathbf{s}$ that are to be prevented in the reconstructed profile. The effect of F on the reconstructions can be adjusted by varying the value of α. The conductivity being discrete, the regularisation function is usually expressed as:

$$F(\mathbf{s}) = \left\| L\mathbf{s} \right\|_2^2 \tag{12}$$

where L is the regularisation matrix. The reconstruction is therefore formulated as:

$$\mathbf{s}_{rec} = \arg\min \left\| h(\mathbf{s}) - \mathbf{v} \right\|_2^2 + \alpha \left\| L\mathbf{s} \right\|_2^2 \tag{13}$$

Regularisation methods mostly achieve the stability of the inversion by penalizing sudden variations in the conductivity, hence offering a trade-off between stability of the reconstruction and sharpness of image. Thorough discussions on the choice of α and on regularisation techniques in ERT can be found in [Kol01] and [Bor02].

ERT testing cell: geometry, size and disposition of electrodes

Spatial resolution and accuracy of ERT reconstructions are constrained from computational aspects (type of algorithm and refinement of the mesh of the numerical models) and from experimental set ups (number, size, geometry and spacing of electrodes used).

[Com08] reports that the total number of independent measurements N of a tomographic reconstruction is:

$$N = \frac{n(n-1)}{2} \tag{14}$$

where n is the number of available electrodes.

A trade off in the design of ERT cells concerns the size of the electrodes [Dam09]. Better definition of the electrical problem is achieved when injecting electrodes have a large surface, generating an even current density, and measuring electrodes are small, providing punctual measurements. Since in ERT electrodes work in turn to inject current and to measure voltage, a compromise is needed. For 2D ERT reconstructions of cylindrical bodies, [Lee10] suggests dimensionless ratios:

$$\frac{W}{D} \approx \frac{\pi}{2n} \text{ and } \frac{L}{D} \approx 0.4 \tag{15}$$

where W is the width of the electrode, D is the diameter of the cell and L is the length of the electrode. These ratios were evaluated based on Finite Element Method simulations of synthetic problems. Anyway, it could be not so strictly necessary to comply rigorously with all of them, also depending on the characteristics of the software used for inversion / reconstruction (e.g. if this introduces complete electrode model [Som92] and if it can model steep gradients).

Finally, measurement protocol can rely on different configuration. Two of them are: (i) the adjacent electrode scheme and (ii) the opposing electrode scheme [Vau97]. Figure 8 shows the current lines obtained with these two configurations under the hypothesis of a homogeneous body. The adjacent electrode configuration, confining

the current towards the cell walls, is more sensitive along the boundaries and loses sensitivity at the centre of the cell. The opposing electrode configuration, providing a more homogenous distribution of electrical current, has a more homogeneous sensitivity.

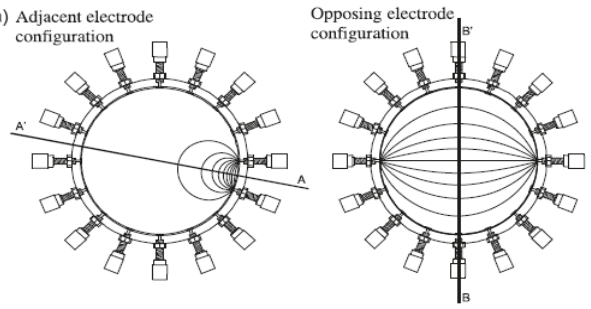

Figure 8: Adjacent electrode and opposing electrode configuration, applied to a cylindrical sample [Dam09].

Even with the opposite electrode configuration, sensitivity of the reconstruction is generally low when anomalies are located towards the centre of the cell [Dam09]. In many cases [Bor05, Lov05, Com08, Dam09] the image of the object is satisfactorily reproduced, but the electrical conductivity values found are not necessarily correct. This depends both on the regularisation technique used and on the ERT system geometry [Dam09]: actually, some very good quantitative results can be obtained if variations of the electrical conductivity in space are not too dramatic. From a practical perspective, quantitative evaluations are easier to be achieved in the case of variations of porosity than in the case of fractures.

ERT testing cell: components

An ERT testing cell is made of a Personal Computer (PC), a data acquisition system, an inverter and a measuring cell. Figure 9 refers to the system used in [Bor05]. A digital direct synthesiser is used for the generation of the AC waveform, which is then fed to a voltage controlled current source and applied via a multiplexer to the pair of driving electrodes. High output impedance of the current source is desirable to drive currents in very resistive media. The injected current intensity is measured on a shunt resistor in series with the driving pair, which ensures accurate measurement of the applied current. A second multiplexer connects the electrodes to an Analogical Digital Converter (ADC), for voltage measurement. The output signals are processed by an on-board Digital Signal Processor which separates in phase and out of phase components. The instrument is controlled by a PC to implement the measurement scheme and to gather the results.

Figure 10 shows the double mesh used in the inversion of tests used in [Com05a] and [Bor05]. A coarse mesh (Figure 10a) has been used to represent the discrete conductivity, while a second finer mesh has been used to represent the electric potential. The number of elements of the coarse mesh coincided with the number of unknowns of the reconstruction process; hence it was chosen considering the number of available measurements in the light of sensitivity and non uniqueness issues. Since such a mesh is not appropriate for an accurate solution of the forward problem, a second and finer mesh was used for the computation of simulated voltages at the electrodes: the fine mesh (Figure 10b) is an adaptive refinement of the coarse mesh.

Further details concerning the experimental set up and the implementation of ERT to laboratory geotechnical studies in available in [Com05a].

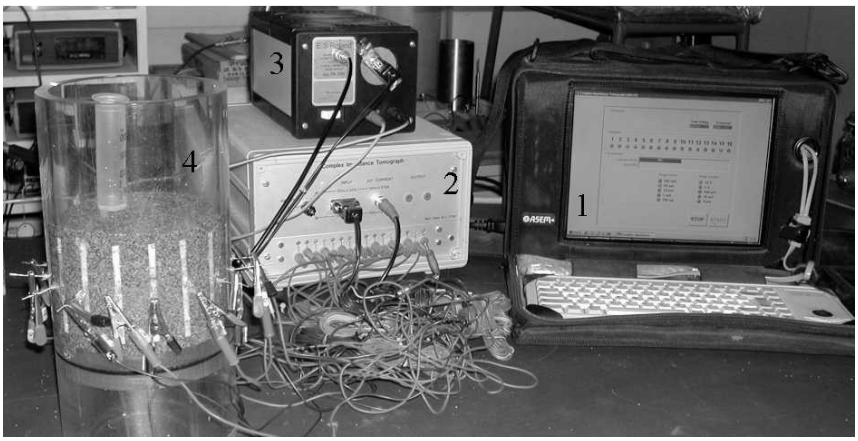

Figure 9: 2D ERT testing cell: 1 Personal Computer 2 Data acquisition system 3 Inverter 4 Measuring Cell [Bor05].

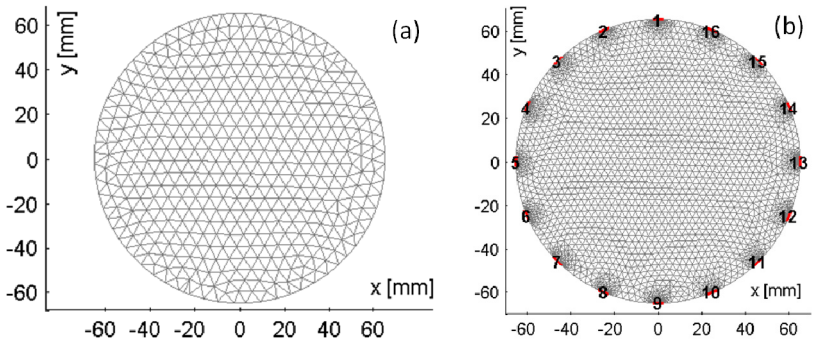

Figure 10: Double mesh used by [Bor05]: (a) mesh of the discrete conductivity (b) refined mesh for the accurate solution of the forward problem.

3.3 Selected ERT studies

Different geometries and spacings between electrodes have been adopted, depending of the desired scale of investigation (see Table 1). It emerges that in some studies ERT ('microresistivity') has been applied to recover information concerning the fabric of the specimens, while in others, with lower resolution, mostly to check local porosity variations or possibility to track transport of fluid or salt.

Table 1: Selected applications of resistivity tomography in the laboratory

Study	Electrodes/ Geometry	Resolution/ measurements per image (m.p.i.)	Objective / Results
[Jac90]	64 sprung gold plated electrodes 5 mm diam / 10 mm spacing	5 mm	Investigating meso structure and fractures. Comparison with down – hole electrical imaging tools.
[Bri98]	2880 electrode grid 5 mm spacing	5 mm	Comparison with X ray radiographs. Investigation of fabric/tortuosity through back analysis of the formation factor F^*
[Jac02]	576 electrodes 10 mm length 5 mm penetration all electrodes on one side of the sample	5 mm 2000 m.p.i. (2D) 8000 m.p.i. (3D)	Comparison with X ray radiographs. Investigation fabric/tortuosity through back analysis of the formation factor F^*
[Lov05]	Injecting electrodes on opposite sides of sample / measuring electrodes on sample surface	5 mm same as down-hole electrical imaging tools	Investigation of depth of fractures / fracture distribution.
[Bin96]	12 equally spaced electrodes on the sidewall of a 320 mm diameter column 4 planes	25 mm (1% total area) 400 m.p.i	Qualitative tracement and flow path of tracer in an undisturbed soil column. Detection of area with higher clay content and of small stones.
[Bor05]	16 electrodes on the circumference of a 130 mm column Electrodes 5 mm wide and 100 mm long.	≈ 10 mm (pixel side) 96 m.p.i.	Validation of the technique. Detection of heterogeneities due to spatial variations of porosity and of composition of the solid phase (cm scale).
[Dam09]	16 electrodes on circumference of 139 mm diameter tube. Electrodes are 7 mm wide and 70 mm long.	≈ 10 mm Sensitivity depends on position of anomalies (decreases if anomaly is at the sample centre)	Validation of the technique / diffusion from a punctual source.
[Com10]	3D EIToedometer 16 electrodes on the sample circumference 13 electrodes on the base 13 electrodes on the top	≈ 5 mm (voxel side) 788 m.p.i.	Changes in water content. Local changes in porosity during mechanical consolidation.

Studies focusing on material fabric have been conducted mostly using electrodes placed over planar surfaces with spacing of about 5 mm. Studies focusing on material heterogeneity and on transport processes have been dome on larger samples, with electrodes usually placed on the external circumference of the sample at spacing of the order of 20-30 mm.

Microresistivity for fabric studies

[Bri98] and [Jac02] showed interesting applications of microresistivity to characterise the fabric of seafloor sediments and rock cores. The heterogeneity of samples of sediments and carbonate rocks was investigated by joint use of X-radiography and microresistivity tomography. In these works resolution of the two techniques was different (0.43 mm / pixel for the Xray, 5 mm / pixel for the microresistivity): data were transformed to an intermediate scale of 1 mm/pixel to make them comparable [Bri98]. X-radiographs underwent nearest-neighbor resampling. Microresistivity data were formed into 1mm/ pixel scale by Kriging.

X radiographs were interpreted to provide density maps (Figure 11a) and microresistivity data were interpreted to provide maps of the formation factor (Figure 11b).The formation factor F^* was evaluated as:

$$F^* = \frac{\chi_w}{\chi_t} \tag{16}$$

where χ_w is the electrical conductivity of the pore water and χ_t is the local electrical conductivity of the sample as estimated by microresistivity.

Knowing the specific density allows deriving porosity maps from density maps (Figure 11c) and information from the two techniques is finally merged to define a map of Archie's exponent m (Figure 11d). This last step is obtained introducing Archie's law:

$$F^* = n^{-m} \tag{17}$$

Archie's exponent reflects the effects on the electrical conductivity of the medium that cannot be explained simply by porosity. Then m can be related to tortuosity [Bri98] or to pore shape and structure [Jac02].

For instance [Bri98] related zones where m is close to one (layer B in Figure11d) to a pelletised volumetric pore structure (see section 2.1) with well-developed connectivity in the direction current flow during electrical measurements. This structure is associated to development of biogenic gas after sediment deposition that migrated in vertical direction. Higher m values in layer A were related to silt/sand storm laminae.

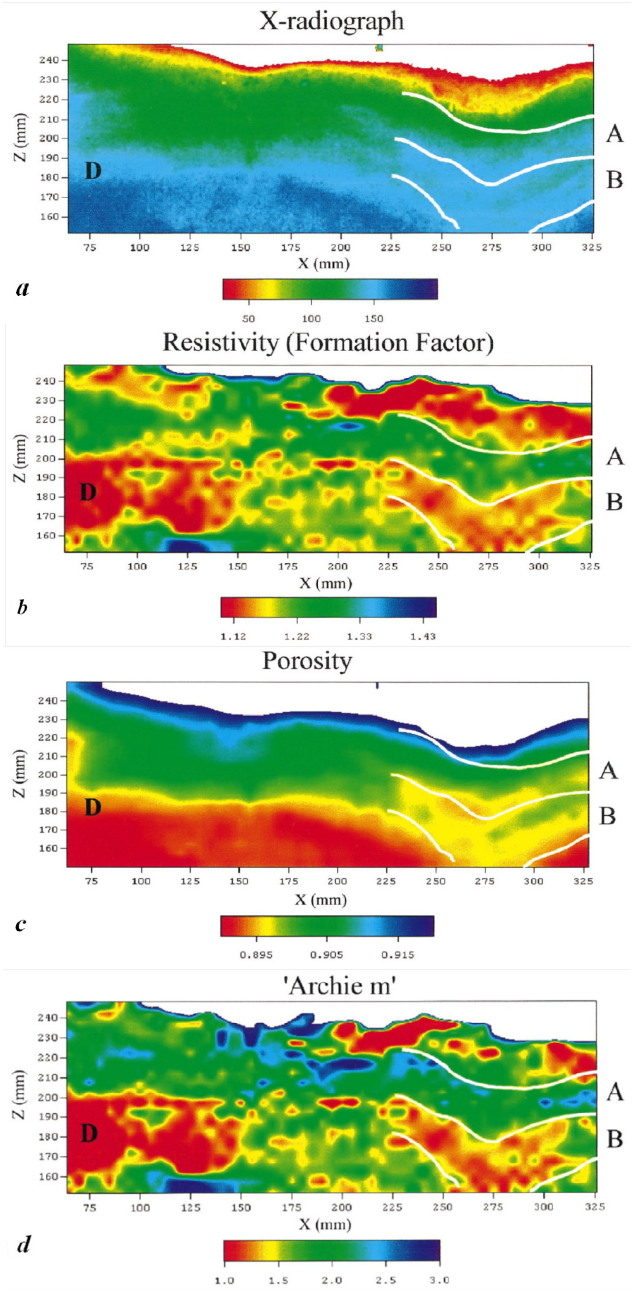

Figure 11: Joint use of X radiographs and microresistivity to characterise fabric and heterogeneity of sediment samples [Bri98].

ERT for porosity and mineralogy heterogeneity studies

In most studies related to hydrogeologic and geotechnics applications, ERT measurements had a resolution of around 10 mm. ERT has then been used to evidence porosity and mineralogy heterogeneities at higher scales, together with monitoring hydro chemical processes [Dam09, Com10]. Figure 12 refers to the experimental results of [Com05b] for the detection of clay fraction inclusions within a sand matrix. Areas where a clay fraction is present are evidenced as areas of higher conductivity. This higher conductivity is explained in terms of contribution of the surface conductivity to the electrical conductivity of clays, a contribution not present in sand.

Shape and position of the conductive inclusions are correctly evaluated and the accuracy of the geometric pattern is actually governed by the size of the element of the FEM mesh. Quantitative evaluation of the local electrical conductivity is not reliable in presence of sharp electrical gradients (as shown in Figure 12a and 12b). It can be noticed that in the reconstructions the sand portion around the kaolin cylinders seems to have a higher electrical conductivity than the remaining sand. This is clearly an artefact, since the sand was prepared homogeneously. Reason for this artefact comes mainly from the regularisation term in the inversion algorithm (Equation 13), that was chosen so to favour stability of the solution rather than its accuracy.

In practical terms, quantitative estimation can anyway be attempted, provided that gradients in the electrical conductivity of the investigated body are relatively modest. Figure 13 shows the interpretation of a test where Ticino sand was prepared at two different densities [Bor05]. Sand was compacted at porosity $n \approx 0.43$ within the cylinder (inclusion) evidenced as a dotted circle in Figure 13a and at porosity $n \approx 0.48$ outside that cylinder. Differences between local values of electrical conductivity appreciated in the ERT reconstruction are very small. Average porosities were then estimated on basis of reconstructed conductivity, since the electrical conductivity of the pore water was independently measured and Archie's exponent m was imposed equal to 1.5. Estimated values were $n \approx 0.42$ for the inclusion and $n \approx 0.46$ for the rest of the sample: such types of results pave the way for the quantitative use of ERT for local evaluations during hydro-chemo-mechanical tests.

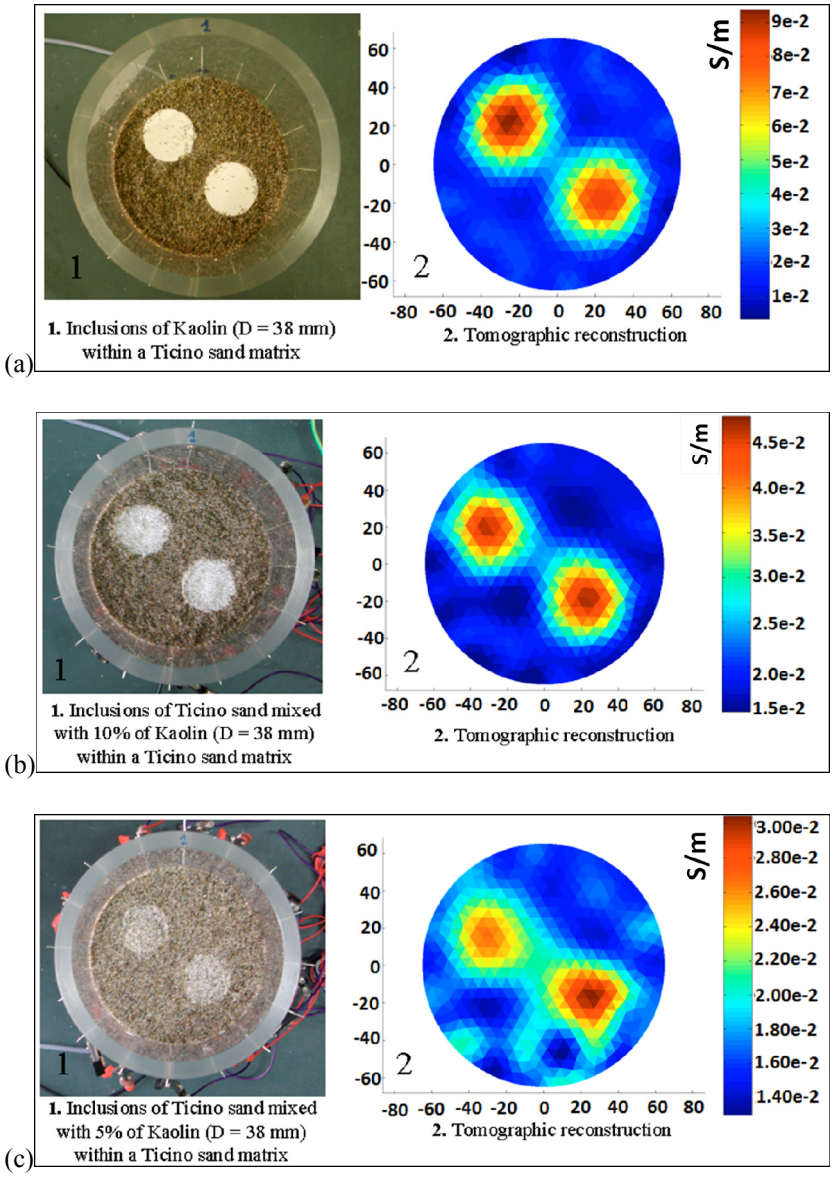

Figure 12: ERT maps of soil electrical conductivity of sand samples with inclusions of clay [Com05b] (axis units are mm).

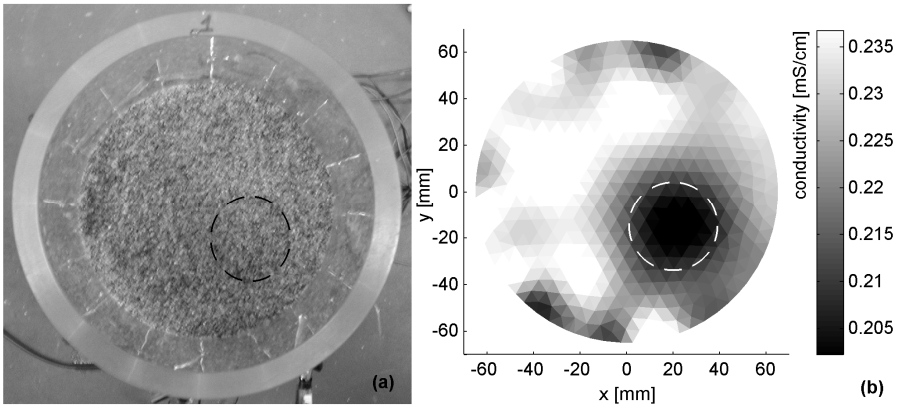

Figure 13: Cylindrical inclusion of compacted sand within a loose sand sample (a); ERT reconstruction (b) [Bor05].

4 Acknowledgements

Guido Musso thanks Cesare Comina (Università degli Studi di Torino) and Sebastiano Foti (Politecnico di Torino) for the joint work aimed at developing and performing ERT tests at laboratory scale at Politecnico di Torino.

5 References

[Abe99] Abell, A.B., Willis, K.L. & Lange, D.A. Mercury intrusion porosimetry and image analysis of cement-based materials. *Journal of Colloid and Interface Science*, *211, 39-44*, 1999.

[Abr04] Abramoff, M.D., Magalhaes, P.J., and Ram, S.J. Image processing with image. *J. Biophotonics International, 11(7), 36-41*, 2004.

[Ahm74] Ahmed, S., Lovell, C.W. & Diamond, S. Pore sizes and strength of compacted clay. *J. Geotech. Eng. Div., ASCE, 100(4), 407-425*, 1974.

[Air10] Airò Farulla, C., Ferrari, A. & Romero. Volume change behaviour of a compacted scaly clay during cyclic suction changes. *Canadian Geotechnical Journal, 47(6), 688-703*, 2010. DOI: 10.1139/T09-138

[Aït04] Aït-Mokhtar, A., Amiri, O., Dumargue, P. & Bouguerra, A. On the applicability of Washburn law: study of mercury and water flow properties in cement-based materials. *Materials and Structures*, *37, 107-113*, 2004.

[AlM96] Al-Mukhtar, M. Belanteur, N. Tessier D. & Vanapalli, S.K. The fabric of clay soil under controlled mechanical and hydraulic stresses. *Applied Clay Science, 11(2-4), 99-115,* 1996.

[And12] Andò, E., Hall, S.A., Viggiani, G., Desrues, J. & Bésuelle, P. Grain-scale experimental investigation of localised deformation in sand: a discrete particle tracking approach. *Acta Geotechnica, 7(1), 1-13,* 2012. DOI: 10.1007/s11440-011-0151-6.

[Aun01] Aung, K.K., Rahardjo, H., Leong, E.C. & Toll, D.G. Relationship between porosimetry measurement and soil-water characteristic curve for an unsaturated residual soil. *Geotechnical and Geological Engineering, 19, 401-416*, 2001.

[Bak90] Baker, J.M. & Allmaras, R.R. System for automating and multiplexing soil moisture measurement by time-domain reflectometry. *Soil Sci. Soc. Am. J., 54(1), 1-6*, 1990.

[Bak95] Baker, J.C., Grabowska-Olszewska, B. & Uwins, P.J.R. ESEM study of osmotic swelling of bentonite from Radzionkow (Poland). *Applied Clay Science, 9, 465-469,* 1995.

[Bar51] Barrett, E.P., Joyner, L.G. & Halenda, P.P. (1951). The determination of pore volume and area distributions in porous substances. I. Computations from nitrogen isotherms. J. Am. Chem. Soc. 1951, 73 (5), 373–380.

[Bés06] Bésuelle, P., Viggiani, G., Lenoir, N., Desrues, J. & Bornert, M. X-ray micro CT for studying strain localization in clay rocks under triaxial compression. *Advances in X-ray tomography for geomaterials*. J. Desrues, G. Viggiani & P. Bésuelle (eds.). ISTE Ltd, London, UK, 35-52, 2006.

[Bev91] Bevc, D., Morrison, H.F. Borehole-to-surface electrical resistivity monitoring of a salt water injection experiment. *Geophysic, 56, 769–777*, 1991.

[Bin96] Binley A., Henry-Poulter S. and Shaw B. Examination of solute transport in an undisturbed soil column using electrical resitance tomography. *Water Resources Research, 32(4), 763-769,* 1996.

[Bor02] Borsic A., Lionheart W. R. B. and McLeod C. N. Generation of anisotropic-smoothness regularisation filters for EIT. *IEEE Transactions on Medical Imaging, 21(6), 579-587*, 2002.

[Bor05] Borsic, A., Comina, C., Foti, S., Lancellotta, R. & Musso, G. Imaging heterogeneities with electrical impedance tomography: laboratory results. *Géotechnique, 55(7), 539-547*, 2005.

[Bre90] Breckon W. R. *Image Reconstruction in Electrical Impedance Tomography*, PhD thesis, Oxford Brookes Polytechnic, 1990.

[Bri98] Briggs, K.B., Jackson, P.D., Holyer R.J., Flint R.C., Sandidge, J.C. and Young, D.K. Two-dimensional variability in porosity, density, and electrical resistivity of Eckernförde Bay sediment. *Continental Shelf Research, 18, 1939-1964,* 1998.

[Car06] Carminati, A., Kaestner, A., Hassanein, R. & Koliji, A. Hydraulic properties of aggregate-aggregate contacts. *Advances in X-ray tomography for geomaterials.* J. Desrues, G. Viggiani & P. Bésuelle (eds.). ISTE Ltd, London, UK, 325-331, 2006.

[Cas92] Cases, J.M., Beraend, I., Besson, G., Francois, M., Uriot, J.P., Thomas, F. & Poirer, J.E. Mechanism of adsorption and desorption of water vapor by homoionic montmorillonite I. The sodium exchanged form. *Langmuir, 8, 2730–2739,* 1992.

[Com05a] Comina C. Imaging Heterogeneities and Diffusion in sand Samples - Electric and Seismic methods. Phd Thesis, Politecnico di Torino, Torino, 2005.

[Com05b] Comina C., Foti S, Lancellotta R, Musso G. and Borsic A. Imaging heterogeneities and diffusion in sand samples. *Proceedings of the XIth IACMAG,* Torin, 27-34, 2005.

[Com08] Comina, C., Foti, S., Musso, G. & Romero, E. EIT oedometer - an advanced cell to monitor spatial and time variability in soil with electrical and seismic measurements. *Geotechnical Testing Journal, 31(5), 404-412*, 2008. DOI: 10.1520/GTJ101367

[Com10] Comina C., Cosentini R.M., Foti S. and Musso, G. Electrical Tomography as laboratorymonitoring tool. *Rivista Italiana di Geotecnica, 1, 9-20,* 2010.

[Cos12] Cosentini, R.M., Della Vecchia, G., Foti, S. & Musso, G. Estimation of the hydraulic parameters of unsaturated samples by electrical resistivity tomography. *Géotechnique, 62(7), 583-594,* 2012. DOI: 10.1680/geot.10.P.0662012

[Dai92] Daily, W.D., Ramirez, A.L., LaBrecque, D.J., and Nitao, J. Electrical resistivity tomography of vadose water movement. *Water Resour. Res., 28, 1429–1442,* 1992.

[Dam09] Damasceno, V.M., Fratta, D. & Bosscher, P.J. Development and validation of a low-cost electrical tomographer for soil process monitoring. *Canadian Geotechnical Journal, 4, 842-854,* 2009.

[Dan93] Danilatos, G.D. Introduction to the ESEM instrument. *Microscopy Research and Technique, 25, 354-361,* 1993.

[Del82] Delage, P., Tessier, D. & Audiguier, M.M. Use of the cryoscan apparatus for observation of freeze-fractured planes of a sensitive Quebec clay in scanning electron microscopy. *Canadian Geotechnical Journal,19, 111-114*, 1982.

[Del84a] Delage, P. & Lefebvre, G. Study of the structure of a sensitive Champlain clay and of its evolution during consolidation. *Canadian Geotechnical Journal, 21, 21-35,* 1984.

[Del84b] Delage, P. & Pellerin, M. Influence de la lyophilisation sur la structure d'une argile sensible du Quebec. *Clay Minerals, 19, 151-160,* 1984.

[Del96] Delage, P., Audiguier M., Cui, Y.J. & Howatt, M.D. Microstructure of a compacted silt. *Canadian Geotechnical Journal, 33, 150-158,* 1996.

[Des06] Desrues, J., Viggiani, G. & Bésuelle, P. (Editors). *Advances in X-ray tomography for geomaterials.* ISTE Ltd, London, UK, 2006.

[Dia70] Diamond, S. Pore size distribution in clays. *Clays and clay minerals, 18, 7-23,* 1970.

[Fad96] Fadeev, A.Yu., Borisova, O.R. & Lisichkin, G.V. Fractality of porous silicas: a comparison of adsorption and porosimetry data. *Journal of Colloid and Interface Science, 183, 1-5,* 1996.

[Gar10] Garzón, E., Sánchez-Soto, P.J. & Romero, E. Physical and geotechnical properties of clay phyllites. *Applied Clay Science, 48, 307–318*, 2010.

[Geb06] Gebrenegus, T., Tuller, M- & Muhuthan, B. The application of X-ray computed tomography for characterisation of surface crack networks in bentonite-sand mixtures. *In: Advances in X-ray tomography for geomaterials*. J. Desrues, G. Viggiani & P. Bésuelle (eds.). ISTE Ltd, London, UK, 207-212, 2006.

[Gim97] Giménez, D., Perfect, E., Rawls, W.J. & Pachepsky, Ya. Fractal models for predicting soil hydraulic properties: a review. *Engineering Geology, 48, 161-183,* 1997.

[Hof75] Hoffman, R. A study of the advancing interface. Interface shape in liquid—gas systems. *Journal of Colloid and Interface Science, 50, 228-241,* 1975.

[Jac90] Jackson, P. D., Lovell, M. A., Pitcher, C., Green, C. A., Evans, C. J., Flint, R., and Forster, A. Electrical resistivity imaging of core samples. *In: Advances in core evaluation*. Worthington P.F. (ed.). Gordon and Breach Science Publishers, New York, 365-378, 1990.

[Jac02] Jackson P.D., Briggs. K. B., Flint, R.C., Holyer, R.J. and Sandidge, J.C. Two- and three-dimensional heterogeneity in carbonate sediments using resistivity imaging. *Marine Geology, 182, 55 – 76,* 2002.

[Jom03] Jommi, C. & Sciotti, A. A study of the microstructure to assess the reliability of laboratory compacted soils as reference material for earth constructions. *In: System-based Vision for Strategic and Creative Design*. F. Botempi (ed.). A.A. Balkema, Lisse, 3, 2409-2415, 2003.

[Jua86] Juang, C.H. & Holtz, R.D. A probabilistic permeability model and the pore size density function. *Int. J. Numer. Anal. Meth. Geomech., 10, 543-553,* 1986.

[Kar07] Karpyn, Z.T. & Piri, M. Prediction of fluid occupancy in fractures using network modeling and X-ray microtomography. Part 1: Data Conditioning and Model Description. *Physical Review E, 76, 016315*, 2007. DOI:10.1103/PhysRevE.76.016315.

[Kho12] Khoshbakht, F., Azizzadeh, M., Memarian, H., Nourozi, G. H. and Moallemi, S. A. Comparison of electrical image log with core in a fractured carbonate reservoir. *J. of Petroleum Science and Engineering, 86–87, 289-296,* 2012.

[Kol01] Kolehmainen V. *Novel Approaches to Image Reconstruction in Diffusion Tomography,* PhD thesis, Department of Applied Physics - Kuopio University, 2001.

[Kol06a] Koliji, A., Carminati, A., Kaestner, A., Vulliet, L., Laloui, L., Fluehler, H., Vontobel, P. & Hassanein, R. Experimental study of flow and deformation in aggregated soils using neutron tomography. *Advances in X-ray tomography for geomaterials.* J. Desrues, G. Viggiani & P. Bésuelle (eds.). ISTE Ltd, London, UK, 341-348, 2006.

[Kol06b] Koliji, A., Laloui, L., Cuisinier, O. & Vulliet, L. Suction induced effects on the fabric of a structured soil. *Transport in Porous Media, 64, 261-278*, 2006.

[Kom99] Komine, H., & Ogata, N. Experimental study on swelling characteristics of sand–bentonite mixture for nuclear waste disposal. *Soils and Foundations, 39(2), 83–97,* 1999.

[Kor92] Korvin, G. *Fractal models in the earth sciences*. Elsevier, Amsterdam, 1992.

[Law78] Lawrence, G.P. Stability of soil pores during mercury intrusion porosimetry. *J. Soil Science*, *29, 299-304*, 1978.

[Lee10] Lee, J. Y. and Santamarina, J. C. Electrical Resistivity Tomography in Cylindrical Cells—Guidelines for Hardware Pre-Design. *Geotechnical Testing Journal, 33(1), Paper ID GTJ102366,* 2010.

[Lov05] Lovell, M., Jackson, P., Flint, R. and Harvey, P.K. Fracture mapping with electrical core images. *Geological Society, London, Special Publications, (240), 107-115,* 2005. DOI:10.1144/GSL.SP.2005.240.01.09

[Low04] Lowell, S., Shields, J.E., Thomas, M.A. & Thommes, M. *Characterization of porous solids and powders: Surface area, pore Size and Density*. Springer Netherlands, 2004.

[Lyt78] Lytle, R.J. and Dines, K.A. *An impedance camera: a system for determining the spatial variation of electrical conductivity*. Report UCRL-52413. Lawrence Livermore Lab., Livermore, CA, 1978.

[Man12] Manahiloh, K.N. & Muhunthan, B. Characterizing liquid phase fabric of unsaturated specimens from X-ray Computed Tomography images. *Proc. 2nd European Conf. on Unsaturated Soils*, Napoli, Italy, 20-22 June 2012. Unsaturated Soils: Research and Applications. C. Mancuso, C. Jommi & F. D'Onza (eds.). Springer, Heidelberg, 1, 71-80, 2012.

[Mat95] Matthews, G.P., Ridgway, C.J. & Spearing, M.C. Void space modelling of mercury intrusion hysteresis in sandstone, paper coating, and other porous media. *Journal of Colloid and Interface Science, 171, 8-27,* 1995.

[Mey94] Meyer, K., Lorenz, P., Böhl-Kuhn, B. & Klobes, P. Porous solids and their characterization. Methods of investigation and application. *Cryst. Res. Technol., 29 (7), 903-930,* 1994.

[Mit05] Mitchell, J.K. & Soga, K. *Fundamentals of soil behaviour* (3rd edition). John Wiley & Sons, Inc. New Jersey, 2005.

[Mon03a] Montes-H, G., Duplay, J., Martinez, L. & Mendoza, C. Swelling-shrinkage kinetics of MX80 bentonite. *Applied Clay Science, 22, 279-293,* 2003.

[Mon03b] Montes-H, G., Duplay, J., Martinez, L., Geraud, Y. & Rousset-Tournier, B. Influence of interlayer cations on the water sorption and swelling-shrinkage of MX80 bentonite. *Applied Clay Science, 23, 309-321,* 2003.

[Mor02] Moro, F. & Böhni, H. Ink-bottle effect in mercury intrusion porosimetry of cement-based materials. *Journal of Colloid and Interface Science*, *246, 135-149*, 2002.

[Muk06] Mukunoki, T., Otani, J., Maekawa, A., Camp, S. & Gourc, J.P. Investigation of crack behaviour on cover soils at landfill using X-ray CT. *In: Advances in X-ray tomography for geomaterials*. J. Desrues, G. Viggiani & P. Bésuelle (eds.). ISTE Ltd, London, UK, 213-219, 2006.

[Mus03] Musso, G., Romero, E., Gens, A. & Castellanos, E. The role of structure in the chemically induced deformations of Febex bentonite. *Applied Clay Science, 23, 229-237*, 2003.

[Osi95] Osiensky, J.L., Donaldson, P.R. Electrical flow through an aquifer for contaminant source leak detection and delineation of plume evolution. *Journal of Hydrology, 169, 243–263*, 1995. DOI:10.1016/0022-1694(94)02610-N

[Pen00] Penumadu, D. & Dean J. Compressibility effect in evaluating the pore size distribution of kaolin clay using mercury intrusion porosimetry. *Canadian Geotechnical Journal, 37, 393-405*, 2000.

[Pir07] Piri, M. & Karpyn, Z.T. Prediction of fluid occupancy in fractures using network modeling and X-ray microtomography. Part 2: Results. *Physical Review E, 76, 016316*, 2007. DOI:10.1103/PhysRevE.76.016316

[Pol02] Polydorides N. and Lionheart W. R. B. A Matlab toolkit for three-dimensional electrical impedance tomography: a contribution to the Electrical Impedance and Diffuse Optical Reconstruction Software project. *Meas. Sci. Technol., 13(12), 1871-1883*, 2002.

[Pra85] Prapaharan, S., Altschaeffl, A.G. & Dempsey, B.J. Moisture curve of a compacted clay: mercury intrusion method. *J. Geotech. Engrg., ASCE, 111(9), 1139-1143*, 1985.

[Ree79] Reed, M.A., Lovell, C.W., Altschaeffl, A.G, & Wood, L.E. Frost-heaving rate predicted from pore-size distribution. *Canadian Geotechnical Journal*, *16, 463-472*, 1979.

[Rie12] Riedel, I., Andò, E., Salager, S., Bésuelle, P. & Viggiani, G. Water retention behaviour explored by X-ray CT analysis. *Proc. 2nd European Conf. on Unsaturated Soils*, Napoli, Italy, 20-22 June 2012. Unsaturated Soils: Research and Applications. C. Mancuso, C. Jommi & F. D'Onza (eds.). Springer, Heidelberg, 1, 81-88, 2012

[Rod06] Rodríguez-Rey, A., Ruiz de Argandoña, V.G., Calleja, L., Suárez del Río, L.M. & Velorio, C. Consolidants influence on sandstone capillarity. X-ray study. *Advances in X-ray tomography for geomaterials*. J. Desrues, G. Viggiani & P. Bésuelle (eds.). ISTE Ltd, London, UK, 381-387, 2006.

[Rol05] Rolland, S., Stemmelen, D., Moyne, C & Masrouri, F. Experimental hydraulic measurements in an unsaturated swelling soil using the dual-energy gamma-ray technique. *Proc. Int. Symposium on Advanced Experimental Unsaturated Soil Mechanics*, Trento, Italy, 27-29 June 2005. In: Advanced Experimental Unsaturated Soil Mechanics. A. Tarantino, E. Romero & Y.J. Cui (eds.). Taylor & Francis Group, London, 305-310. 2005.

[Rom99] Romero, E. Gens, A. & Lloret, A. Water permeability, water retention and microstructure of unsaturated Boom clay. *Engineering Geology, 54, 117-127*, 1999.

[Rom08] Romero, E. & Simms, P.H. Microstructure investigation in unsaturated soils: a review with special attention to contribution of mercury intrusion porosimetry and environmental scanning electron microscopy. *Geotechnical and Geological engineering, 26(6), 705-727*, 2008. DOI: 10.1007/s10706-008-9204-5.

[Rom11] Romero, E., Della Vecchia, G. & Jommi, C. An insight into the water retention properties of compacted clayey soils. *Géotechnique, 61(4), 313-328*, 2011. Doi: 10.1680/geot.2011.61.4.313

[Rom12] Romero, E., Senger, R., Marschall, P. & Gómez, R. Air tests on low-permeability claystone formations. Experimental results and simulations. Theme lecture. *Int. Workshop 'AMTSS - Advances in Multiphysical Testing of Soils and Shales'*, EPFL Lausanne (Switzerland), 3 - 5 September 2012.

[Sen09] Sentenac, P. and Zielinski, M. Clay fine fissuring monitoring using miniature geo-electrical resistivity arrays. *Journal Environmental Earth Sciences, 59(1), 205-214*, 2009. DOI:10.1007/s12665-009-0017-5.

[Sil73] Sills, I.D., Aylmore, L.A.G. & Quirk, J.P. A comparison between mercury injection and nitrogen sorption as methods of determining pore size distribution. *Proceedings of the Soil Science Society of America, 37, 535-537,* 1973.

[Sim01] Simms, P.H. & Yanful, E.K. Measurement and estimation of pore shrinkage and pore distribution in a clayey till during soil-water characteristic curve tests. *Canadian Geotechnical Journal, 38, 741-754*, 2001.

[Sim02] Simms, P.H. & Yanful, E.K. Predicting soil-water characteristic curves of compacted plastic soils from measured pore-size distributions. *Géotechnique, 52(4), 269-278*, 2002.

[Sim04] Simms, P.H. & Yanful, E.K. A discussion of the application of mercury intrusion porosimetry for the investigation of soils, including an evaluation of its use to estimate volume change in compacted clayey soils. *Géotechnique, 54(6), 421-426,* 2004.

[Sim05] Simms, P.H. & Yanful, E.K. A pore-network model for hydromechanical coupling in unsaturated compacted clayey soils. *Canadian Geotechnical Journal, 42, 499-514*, 2005.

[Sla97] Slater, L., Binley, A. and Brown, D. Electrical imaging of fractures using ground-water salinity change. *Groundwater 35, 436–442, 1997.*

[Som92] Somersalo, E., Cheney, M. and Isaacson, D. Existence and uniqueness for electrode models for electric current computed tomography. *SIAM J. Appl. Math. 52(4), 1023–1040*, 1992.

[Syl87] Sylvester, J. and Uhlman, G.. A global uniqueness theorem for an inverse boundary value problem. *Ann. Math., 125, 153 – 169,* 1987.

[Tak06] Takahashi, M., Takemura, T., Hirai, H., Murakoshi, A. & Kato, M. Spatial and density resolution in microfocus X-ray CT applied to studies of microstructural changes in rocks with increasing hydrostatic pressure. *In: Advances in X-ray tomography for geomaterials*. J. Desrues, G. Viggiani & P. Bésuelle (eds.). ISTE Ltd, London, UK, 421-427, 2006.

[Vau97] Vauhkonen M. *Electrical Impedance Tomography and Prior Information*. PhD thesis, Kuopio University, 1997.

[Van05] Van Geet, M., Volckaert, G. & Roels, S. The use of microfocus X-ray computed tomography in characterising the hydration of a clay pellet / powder mixture. *Applied Clay Science, 29, 73– 87,* 2005.

[Web97] Webb, P.A. & Orr, C. *Analytical methods in fine particle technology.* Micromeritics Instrument Corp, Norcross, 1997.

[Whi94] White, P.A.. Electrode arrays for measuring groundwater flow direction and velocity. *Geophysics, 59, 192–201,* 1994.